



## Synergistic effect of multiple vacancies to induce lattice oxygen redox in NiFe-layered double hydroxide OER catalysts

Yiyue Zhai<sup>a,1</sup>, Xiangrong Ren<sup>a,1</sup>, Yu Sun<sup>d,1</sup>, Deng Li<sup>a</sup>, Bolun Wang<sup>b,\*</sup>, Shengzhong (Frank) Liu<sup>a,c,\*\*</sup>

<sup>a</sup> Key Laboratory of Applied Surface and Colloid Chemistry, Ministry of Education, Shaanxi Key Laboratory for Advanced Energy Devices, Shaanxi Engineering Lab for Advanced Energy Technology, School of Materials Science and Engineering, Shaanxi Normal University, Xi'an 710119, PR China

<sup>b</sup> State Key Laboratory of Inorganic Synthesis and Preparative Chemistry, College of Chemistry Jilin University, Changchun 130012, PR China

<sup>c</sup> iChEM, Dalian Institute of Chemical Physics, University of Chinese Academy of Sciences, Chinese Academy of Sciences, Dalian 116023, PR China

<sup>d</sup> School of Advanced Materials and Nanotechnology, Xidian University, Xi'an 710126, PR China

### ARTICLE INFO

#### Keywords:

NiFe LDH  
Vacancy defects  
OER  
Electrocatalysis

### ABSTRACT

The role of multiple vacancies containing cation and anion defects in NiFe layered double hydroxide (LDH) is still worth pursuing in electrocatalytic oxygen evolution reaction (OER). Herein, a strategy integrating the oxygen and iron vacancies is proposed to fabricate NiFe LDH with highly efficient OER performance. More Fe vacancies have been introduced with increasing Fe content in NiFe-LDH structure; operando electrochemical characterizations and density functional theory (DFT) calculations reveal that the synergic effect between the iron and the oxygen vacancies promotes the generation of reconstructed active layers, optimizing the adsorption free energy of oxygen-containing intermediates. More importantly, active NiOOH intermediate species induced by oxygen vacancies are associated with OH<sup>-</sup> intercalation pseudocapacitance, activating lattice oxygen during water oxidation. The as-prepared Ni<sub>0.3</sub>Fe<sub>0.7</sub>-LDH@NF showed ultralow overpotentials of 184 and 287 mV to achieve 10 and 400 mA·cm<sup>-2</sup>, respectively. Our work provides a new paradigm for designing high-efficiency OER electrocatalysts.

### 1. Introduction

To meet the urgent need for a low-carbon society, energy from hydrogen obtained via water splitting using renewable energy sources is the leading and greenest way [1–3]. The overall water splitting via electrolysis includes the hydrogen evolution reaction at the cathode side and the oxygen evolution reaction at the anode side, where the sluggish kinetics of the OER at the anode side seriously impedes the activities of catalysts for the overall water splitting [4–7]. The design of efficient catalysts to boost the reaction kinetics in water oxidation is eagerly demanded. Currently, the state-of-art catalysts for the OER are mostly noble metal-based materials, such as IrO<sub>2</sub> and RuO<sub>2</sub>. However, their scarcity and consequential high cost tremendously hamper their practical widespread application in electrocatalytic water splitting [8,9]. Therefore, a large variety of transition metal-based catalysts, which are

low-cost and show comparable activities, have been widely investigated over the last decades [10–12], especially the NiFe layered double hydroxides (LDH) [13–15].

Generally, the excellent OER performance of NiFe LDH under alkaline conditions arises because their surface is prone to undergo significant reconstruction to form γ-NiOOH, which is the actual active species. However, the OER activity of NiFe LDH is highly restricted to a small number of active sites at the edges and limited by weak conductivity [16,17]. Accordingly, numerous efforts including interfacial interaction, vacancy-modifying, and heteroatom-doping have been developed to optimize the OER performance of NiFe LDH [18–21]. The in-situ construction of three-dimensional (3D) hierarchical nanostructures with multiple vacancies on the Ni foam (NF) has been demonstrated as an effective and popular strategy to prepare highly efficient NiFe LDH catalysts [22–24]. The 3D self-supported flexible configuration can

\* Corresponding author.

\*\* Corresponding author at: Key Laboratory of Applied Surface and Colloid Chemistry, Ministry of Education, Shaanxi Key Laboratory for Advanced Energy Devices, Shaanxi Engineering Lab for Advanced Energy Technology, School of Materials Science and Engineering, Shaanxi Normal University, Xi'an 710119, PR China.

E-mail addresses: [wangbolun@jlu.edu.cn](mailto:wangbolun@jlu.edu.cn) (B. Wang), [szliu@dicp.ac.cn](mailto:szliu@dicp.ac.cn) (S.F. Liu).

<sup>1</sup> These authors contributed equally to this work.

effectively accelerate mass transport and gas release, benefiting from the high specific area and open-pore structure of NF. Furthermore, the binder-free method provides intimate integration between the electrocatalyst and NF, which would facilitate the charge transfer and maintain stability at high current densities [16].

In parallel with the above tactics, vacancy engineering has also been confirmed supportive for electrocatalytic water splitting. To be specific, oxygen vacancies ( $O_v$ ) can significantly facilitate the adsorption of hydroxide ions and modify the adsorption free energy of oxygen-containing intermediate species; meanwhile, metal vacancies could produce abundant unsaturated coordination sites and high-energy

dangling bonds, further modulating the local electronic configurations around active metal sites and hence promoting the activity for oxygen evolution [6,25–28]. An integration of the oxygen and metal vacancies in the NiFe LDH catalysts would thus be promising due to the synergy of these effects for enhancing OER activity [17,19]. However, a detailed understanding of the synergistic effects of the metal and oxygen vacancies on the mechanism of water oxidation over NiFe LDH is still elusive.

Herein, we intentionally introduce metal and oxygen vacancies in NiFe LDH catalysts by fabricating NiFe LDH nanosheets with controlled Ni/Fe ratios. The NiFe LDH nanosheets were grown on the porous NF via

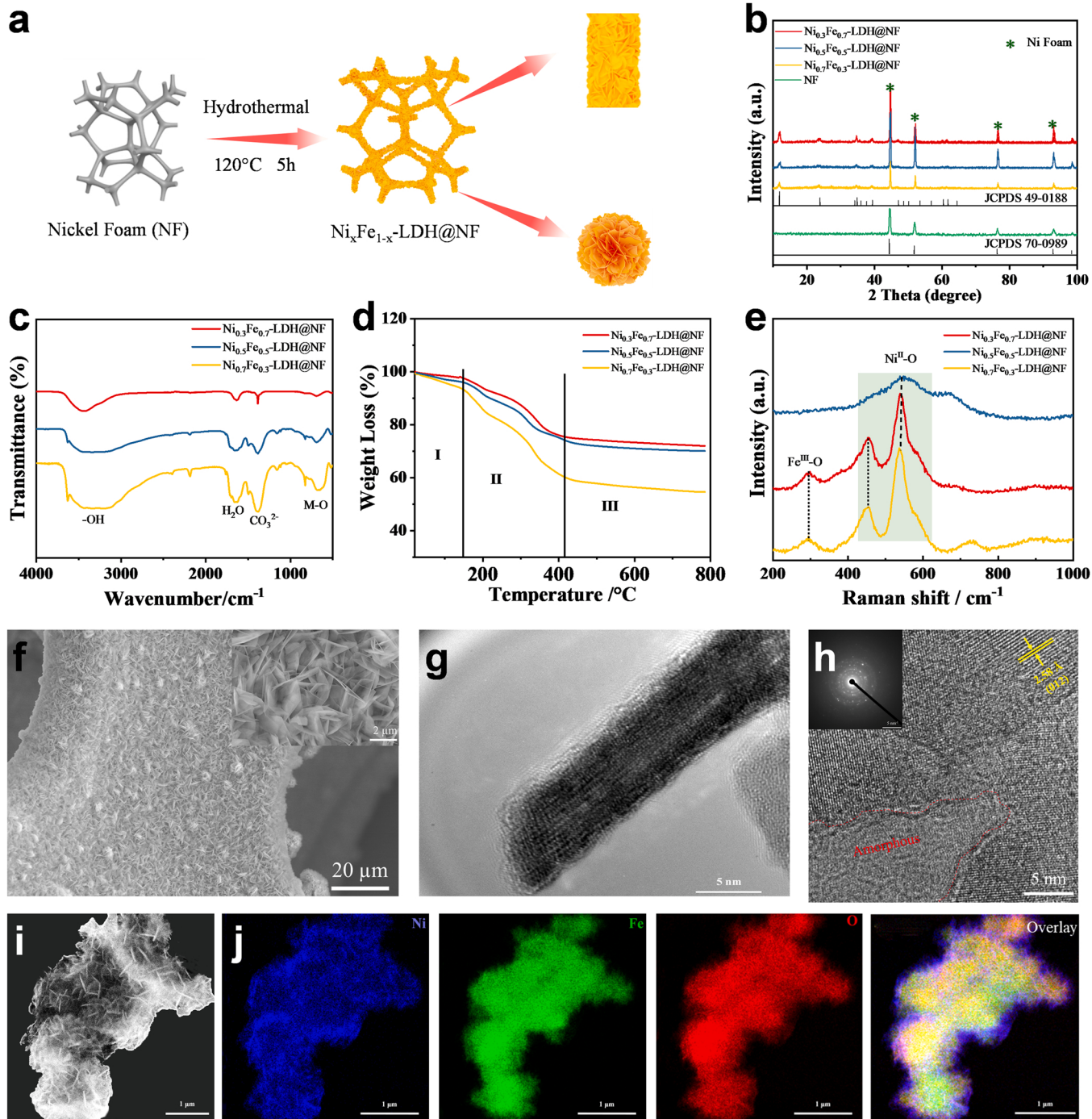


**Fig. 1.** (a) Schematic representation of the synthesis procedure for  $Ni_xFe_{1-x}$ -LDH@NF ( $x = 0.3, 0.5$  and  $0.7$ ). (b) XRD patterns, (c) FT-IR spectra, (d) TGA curves, and (e) Raman spectra of  $Ni_xFe_{1-x}$ -LDH@NF ( $x = 0.3, 0.5$  and  $0.7$ ). (f) SEM image, (g) TEM image, (h) HR-TEM image, and (i,j) Elemental mapping of  $Ni_{0.3}Fe_{0.7}$ -LDH@NF. Inset of (h): SAED pattern.

a simple one-step hydrothermal method, where these nanosheets formed a unique 3D hierarchical nanostructure with a large number of edge sites and strong structural integrity. The synergic effect of multiple vacancies not only modulates the electronic state of the NiFe-LDH for prompting the reconstruction of the active  $\gamma$ -NiOOH phase but also triggers lattice oxidation with the assistance of oxygen-vacancy-mediated redox pseudocapacitance during the OER process. As a result, the  $\text{Ni}_{0.3}\text{Fe}_{0.7}$ -LDH@NF exhibited remarkable OER performance with an ultralow overpotential of 184 mV to deliver 10 mA·cm<sup>-2</sup>, together with excellent durability for continuous operation at 100 mA/cm<sup>2</sup>, outperforming most reported catalysts.

## 2. Experimental section

### 2.1. Materials

Acetone (AR, 99.5%), ethanol (AR, 99.5%), potassium hydroxide (KOH, GR), nickel nitrate hexahydrate ( $\text{Ni}(\text{NO}_3)_2 \cdot 6\text{H}_2\text{O}$ ), iron nitrate nonahydrate ( $\text{Fe}(\text{NO}_3)_3 \cdot 9\text{H}_2\text{O}$ ) and urea ( $\text{CH}_4\text{N}_2\text{O}$ ) were purchased from Sinopharm Chemical Reagent Company. Ammonium fluoride ( $\text{NH}_4\text{F}$ ) and iridium oxide ( $\text{IrO}_2$ ) were obtained via Shanghai Aladdin Biochemical Technology Co Ltd. Nickel foam (NF) was acquired from Kunshan guangshengjia New Material Co., Ltd; the thickness of the nickel foam is 2.0 mm, and its bulk density is 0.3 g·cm<sup>-3</sup>. The deionized (DI) and ultra-pure water were produced by an ultrapure water system. All reagents were utilized without further purification.

### 2.2. Preparation of $\text{Ni}_x\text{Fe}_{1-x}$ -LDH@NF

The preparation of  $\text{Ni}_x\text{Fe}_{1-x}$ -LDH@NF ( $x = 0.3, 0.5$  and  $0.7$ ) is presented in Fig. 1a. Specifically, the NF ( $1 \times 2 \text{ cm}^2$ ) was ultrasonically cleaned in acetone, ethanol, and ultra-pure water for 15 min, respectively. The different mole ratios of Ni and Fe ( $x = 0.3, 0.5$  and  $0.7$ ) were obtained through mixing ( $\text{Ni}(\text{NO}_3)_2 \cdot 6\text{H}_2\text{O}$ ) and ( $\text{Fe}(\text{NO}_3)_3 \cdot 9\text{H}_2\text{O}$ ), where the total number of two metal cation remained at 1.2 mmol. Afterward,  $\text{NH}_4\text{F}$  (92.5 mg) and urea (360 mg) were added and dissolved in DI water of 30 mL to acquire clean solution under constantly stirring for 20 min. Subsequently, the pro-cleaned NF and NiFe precursor solution were transferred to a 50 mL stainless-steel Teflon-lined autoclave and heated at 120 °C for 5 h. Finally, the  $\text{Ni}_x\text{Fe}_{1-x}$ -LDH@NF could be collected after thoroughly rinsed with DI water and dried in an electric oven at 60 °C.

### 2.3. Synthesis of $\text{IrO}_2$ @NF

A homogeneous paste was obtained by 10 mg  $\text{IrO}_2$  powder, 30  $\mu\text{L}$  of 5 wt% of Nafion and a few drops of ethanol, which was supported on 1 cm × 1 cm NF and then pressed at 10 MPa. The as-prepared electrodes were dried at 60 °C for 12 h.

### 2.4. Physicochemical characterizations

X-ray diffractometry (XRD) patterns were taken on a Bruker D8 (Cu K $\alpha$  radiation at 2 °/min). The morphology and elemental analysis of the as-prepared specimen were performed with field emission scanning electron microscopy (SEM) and energy dispersive X-ray spectroscopy (EDS) attached to the SEM (SU-8020). The microstructural information was characterized by transmission electron microscopy (TEM) and high-resolution transmission electron microscopy (HRTEM), and the selected area electron diffraction (SAED) was further employed to identify the crystal structure (JEOL JEM-2800). The valence state and chemical components of the samples were carried out utilizing X-ray photoelectron spectroscopy (XPS, Thermo Scientific ESCALAB 250Xi). Electron spin resonance (ESR) was done by Bruker E500 spectrometer. The Brunauer-Emmett-Teller (BET) specific surface areas were determined by a Micro ASAP (2020) analyzer. The Barrett-Joyner-Halenda (BJH) method was chosen to calculate the pore size distribution. The Fourier

transform infrared (FT-IR) spectra and Raman spectra were recorded by Vertex70 of Bruker and Via-Reflex of Renishaw, separately.

The X-ray absorption fine structure spectra (Ni K-edge and Fe K-edge) were collected at BL14W beamline in Shanghai Synchrotron Radiation Facility (SSRF). The storage rings of SSRF were operated at 3.5 GeV with a stable current of 200 mA. Using Si (111) double-crystal monochromator, the data collection was carried out in fluorescence mode using Lytle detector. All spectra were collected in ambient conditions.

### 2.5. Electrochemical measurements

A standard three-electrode system in  $\text{O}_2$ -saturated 1 M KOH was employed to estimate the OER activity via utilizing CHI660E electrochemistry workstation, where  $\text{Ni}_x\text{Fe}_{1-x}$ -LDH@NF ( $x = 0.3, 0.5$  and  $0.7$ ) and  $\text{IrO}_2$ @NF were directly used as the working electrodes, a Hg/HgO electrode and a Pt foil were exploited as reference electrode and counter-electrode, respectively. The high-purity  $\text{O}_2$  was employed to purge the system before the OER, and further maintain the bubbling throughout the electrochemical experiment. All the potentials were calibrated versus reversible hydrogen electrode (RHE) via the equation of  $E_{\text{RHE}} = E_{\text{Hg/HgO}} + 0.0592 \text{ pH} + 0.098 \text{ V}$ .

Besides, compensation of  $iR_s$  drop of each polarization curve with 90% was automatically performed by the electrochemical workstation. Cyclic voltammetry (CV) measurements were conducted with different scanning rates. Linear sweep voltammetry (LSV) curves were collected at a constant rate of 5 mV·s<sup>-1</sup>, and Tafel slopes were given by fitting the linear part of overpotential versus current density in log scale ( $\log |j|$ ). Electrochemical impedance spectroscopy (EIS) was measured at 1.43 V versus RHE within frequency window ranging from  $10^5$  Hz to  $10^{-2}$  Hz with an amplitude of 5 mV. The electrochemical surface areas (ECSA) were investigated by CV method measuring the current related to double-layer capacitance ( $C_{dl}$ ) in a non-Faradic potential window. Typically, the potentials were swept between 1.125 V<sub>RHE</sub> and 1.225 V<sub>RHE</sub> under different scan rates (1–10 mV·s<sup>-1</sup> and 10–100 mV·s<sup>-1</sup>). Then, the  $C_{dl}$  was determined by plotting the  $\Delta j$  ( $j_a - j_c$ ) at 1.175 V<sub>RHE</sub> against the scan rate. The gaseous products of overall water splitting were monitored in real time by an on-line gas chromatograph. The faradic efficiency (FE) was obtained according to Eq. (1):

$$\text{FE} = (m \times n \times F) / (I \times t) \quad (1)$$

Where  $m$  is produced moles of oxygen or hydrogen (mol),  $n$  is the number of transfer electrons,  $F$  is the Faraday constant (96485.33 C/mol),  $I$  is the given current density (A/cm<sup>2</sup>), and  $t$  is reaction time.

### 2.6. Theoretical calculations

First-principles calculations were carried out on the basis of periodic DFT using a generalized gradient approximation within the Perdew-Burke-Ernzerhof exchange correction functional. We used the projector-augmented wave method for describing ionic cores as implemented in the Vienna ab initio simulation package (VASP). The wave functions were constructed from the expansion of plane waves with an energy cutoff of 500 eV. Gamma centered k-point of  $3 \times 3 \times 1$  have been used for geometry optimization. The consistence tolerances for the geometry optimization are set as  $1.0 \times 10^{-5}$  eV/atom for total energy and 0.05 eV/Å for force, respectively. In order to avoid the interaction between the two surfaces, a large vacuum gap of 20 Å has been selected in the periodically repeated slabs. In free energies calculations, the entropic corrections and zero-point energy (ZPE) have been included.

The free energy of species was calculated according to the standard formula:

$$\Delta G = E + \Delta ZPE + \Delta H - \Delta TS \quad (2)$$

where ZPE was the zero-point energy,  $\Delta H$  was the integrated heat

capacity, T was the temperature of product, and S was the entropy.

### 3. Results and discussion

#### 3.1. Structural characterizations

A series of 3D hierarchical  $\text{Ni}_x\text{Fe}_{1-x}\text{-LDH@NF}$  ( $x = 0.3, 0.5$  and  $0.7$ ), labeled  $\text{Ni}_{0.3}\text{Fe}_{0.7}\text{-LDH@NF}$ ,  $\text{Ni}_{0.5}\text{Fe}_{0.5}\text{-LDH@NF}$  and  $\text{Ni}_{0.7}\text{Fe}_{0.3}\text{-LDH@NF}$ , respectively, were prepared by a one-step hydrothermal method, as schematically displayed in Fig. 1a. Briefly, the total number of corresponding metal nitrates remained at  $1.2\text{ mmol}$  to achieve different molar ratios of Ni and Fe, and afterward, urea served as a precipitant to regulate the pH of the solution and slowly released  $\text{OH}^-$  and  $\text{CO}_3^{2-}$  ions over the hydrolysis reaction, while the  $\text{F}^-$  released from the  $\text{NH}_4\text{F}$  could activate the NF to form more active sites for nucleation and growth of NiFe LDH, favoring the intimate interaction between the active sites and NF. In addition, different amounts of the  $\text{NH}_4\text{F}$  can

induce different morphologies owing to the key role of  $\text{F}^-$  anions in controlling the nucleation rate of NiFe LDH precursor [29–31].

The XRD results of the as-prepared samples are displayed in Fig. 1b, where the major diffraction peaks at  $44.61^\circ$ ,  $51.98^\circ$  and  $76.59^\circ$  (marked with green stars) are indexed to the (111), (200) and (220) facets of NF (JCPDS No. 70-0989), while the diffraction peaks centered at  $11.88^\circ$ ,  $23.67^\circ$ ,  $34.78^\circ$ ,  $39.38^\circ$  and  $60.21^\circ$  matched well with the (003), (006), (012), (015) and (110) crystal planes of NiFe LDH (JCPDS No. 49-0188) [32]. This indicated that the NiFe LDH catalysts were successfully grown on the Ni foam. Furthermore, the functional groups of the samples were investigated through the Fourier transform infrared (FT-IR) spectra shown in Fig. 1c. The vibration peaks at  $3439$ ,  $1631$ ,  $1383$  and  $689\text{ cm}^{-1}$  were observed, which can be assigned to  $-\text{OH}$ ,  $\text{H}_2\text{O}$ ,  $\text{CO}_3^{2-}$  and M-O, respectively [33]. The formation of interlayered anions including  $\text{OH}^-$  and  $\text{CO}_3^{2-}$  is thus confirmed. The thermogravimetric (TG) profiles are given in Fig. 1d, where the weight loss mode can be separated into two stages. The one in the range from  $40^\circ\text{C}$  to  $150^\circ\text{C}$  corresponds to the

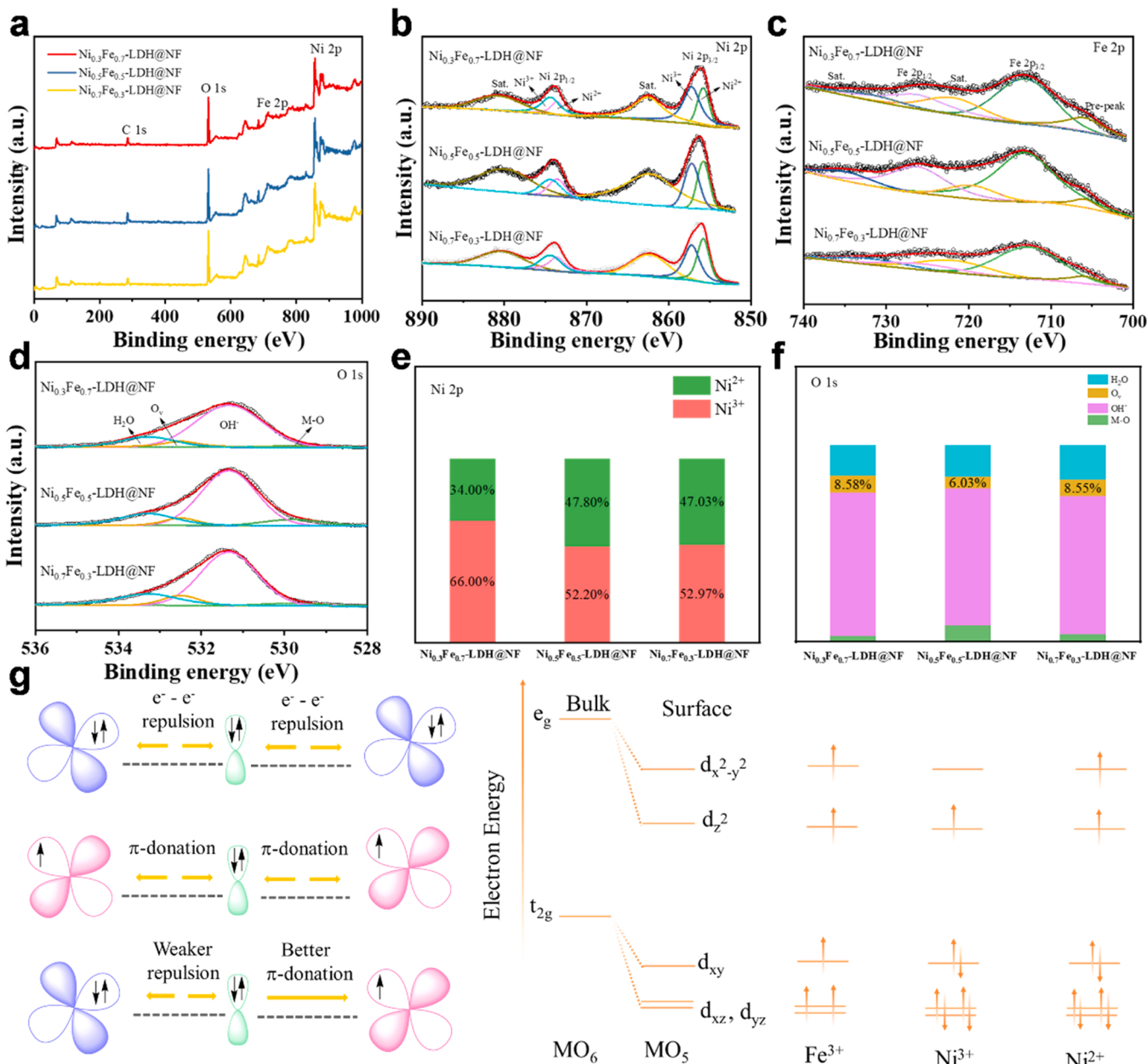


**Fig. 2.** (a) XPS survey spectra, (b) Ni 2p, (c) Fe 2p, and (d) O 1s spectra of  $\text{Ni}_x\text{Fe}_{1-x}\text{-LDH@NF}$  ( $x = 0.3, 0.5$  and  $0.7$ ). (e) The ratio of  $\text{Ni}^{3+}/(\text{Ni}^{2+} + \text{Ni}^{3+})$ . (f) The contribution of different oxygen-containing groups. (g) Schematic representation of the electronic coupling between Ni and Fe.

evaporation of H<sub>2</sub>O of the interlayer and adsorbed water molecules, while the other in the range from 150 °C to 425 °C is the elimination of the -OH and CO<sub>3</sub><sup>2-</sup> from the interlayer, resulting in the LDH-to-spinel transition [34]. Raman spectra of the samples are shown in Fig. 1e, where the peaks at 452 and 536 cm<sup>-1</sup> could be assigned to Ni-O vibrations of defective or disordered Ni<sup>II</sup>-O, while the characteristic peak at 294 cm<sup>-1</sup> is associated with the existence of Fe<sup>III</sup>-O species [35].

The morphologies of Ni<sub>x</sub>Fe<sub>1-x</sub>-LDH@NF ( $x = 0.3, 0.5$  and  $0.7$ ) were further investigated (Fig. S1 and S2). Illustratively, the Ni<sub>0.3</sub>Fe<sub>0.7</sub>-LDH@NF reveals 2D nanosheets grown uniformly onto NF, as depicted in Fig. 1f. The TEM micrograph of Ni<sub>0.3</sub>Fe<sub>0.7</sub>-LDH@NF further confirms the nanosheet feature of Ni<sub>0.3</sub>Fe<sub>0.7</sub> LDH with a partially amorphous structure. Markedly, the distance between lattice fringes is determined to be 0.25 nm, which is in good agreement with the (012) facet of typical NiFe LDH (Fig. 1g,h) [36–38]. Specifically, the amorphous Ni<sub>0.3</sub>Fe<sub>0.7</sub> LDH would provide a higher activity for water oxidation, attributed to the advantage of its flexibility as well as its abundant unsaturated coordination active sites to easily adsorb the reactants, outperforming its counterpart crystalline phases [16]. Apparently, the corresponding EDS mapping (Fig. 1i,j) demonstrated homogeneous distributions of Ni, Fe and O in Ni<sub>0.3</sub>Fe<sub>0.7</sub>-LDH@NF.

The superficial components of Ni<sub>x</sub>Fe<sub>1-x</sub>-LDH@NF ( $x = 0.3, 0.5$  and  $0.7$ ) and their electronic states were further investigated by X-ray photoelectron spectroscopy (XPS). As observed in Fig. 2a, the survey spectra of all specimens confirmed the coexistence of Ni, Fe, O and C elements, in good agreement with the EDS results. Fig. 2b presents the high-resolution curves of the Ni 2p spectra, demonstrating two dominant peaks at binding energies of  $\sim 856.2$  eV and  $873.8$  eV, which can be assigned to Ni 2p<sub>3/2</sub> and Ni 2p<sub>1/2</sub>, respectively. In addition, the broad peaks located at 861.8 and 880.0 eV are ascribed to the typical satellite peaks of Ni 2p<sub>3/2</sub> and Ni 2p<sub>1/2</sub> [8,21,39]. Furthermore, the peak-fitting analysis revealed that there exist two states of Ni 2p, which are Ni<sup>2+</sup>(t<sub>2g</sub><sup>6</sup>e<sub>g</sub><sup>2</sup>) and Ni<sup>3+</sup>(t<sub>2g</sub><sup>6</sup>e<sub>g</sub><sup>1</sup>). Notably, the Ni<sup>3+</sup>(t<sub>2g</sub><sup>6</sup>e<sub>g</sub><sup>1</sup>) approaches the optimal e<sub>g</sub><sup>1,2</sup> electronic configuration, which could form σ-bonds with the adsorbed oxygen during the OER process (Fig. 2g and Fig. S4), and the larger proportion of Ni<sup>3+</sup> could favor the OER activity [24,40]. Strikingly, the Ni<sub>0.3</sub>Fe<sub>0.7</sub>-LDH@NF features the highest percentage of Ni<sup>3+</sup> (66.00%) among all prepared specimens in Fig. 2e, which may be the reason for its exceptional electrocatalytic performance. Regarding the Fe 2p spectra of Ni<sub>x</sub>Fe<sub>1-x</sub>-LDH@NF ( $x = 0.3, 0.5$  and  $0.7$ ) in Fig. 2c, it can be observed that a pair of characteristic peaks at  $\sim 712.6$  and  $725.6$  eV are accompanied by the satellite peaks at 721.8 and 734.8 eV, validating the Fe 2p<sub>3/2</sub> and Fe 2p<sub>1/2</sub> of Fe<sup>3+</sup> (where a single low-intensity peak located on the low-binding-energy side can be found, named as Pre-peak, which accounts for the formation of Fe ions being lower than normal oxidation state by introducing defects in neighboring sites [41]). The deconvolution of the high-resolution O 1 s spectra in Fig. 2d reveals that the discerned peaks at  $\sim 529.8, 531.4, 532.5$  and  $533.3$  eV are attributed to lattice oxygen (M-O), hydroxide (M-OH), oxygen vacancies (O<sub>v</sub>) and surface-adsorbed H<sub>2</sub>O, respectively [42], reflecting a higher content of surface O<sub>v</sub> in Ni<sub>0.3</sub>Fe<sub>0.7</sub>-LDH@NF (Fig. 2f).

Additionally, the slightly positive shift (0.2 eV) of the Ni 2p<sub>3/2</sub> peak with increasing Fe content demonstrates the electronic structure of Ni can be regulated via the introduction of Fe [43]. To be specific, this change is identified to be the partial electron transfer of Ni-to-Fe through the O<sup>2-</sup>. Further, the corresponding electron-transfer mechanism can be interpreted in accordance with the electron configurations shown in Fig. 2g, where the t<sub>2g</sub> of Ni<sup>2+</sup> and Ni<sup>3+</sup> have no unpaired electron, and, hence they could interact with bridging O<sup>2-</sup> by e<sup>-</sup>-e<sup>-</sup> repulsion, hampering the charge transfer. However, there is an unpaired electron of Fe<sup>3+</sup> in the 3d t<sub>2g</sub> energy level, whose major interaction with O<sup>2-</sup> is via π-donation. Under the coupling between Ni<sup>3+</sup> to Fe<sup>3+</sup>, the π-donation of Fe-O would be stronger due to e<sup>-</sup>-e<sup>-</sup> repulsion of Ni-O, which leads to partial electron transfer from Ni<sup>3+</sup> to Fe<sup>3+</sup>, in line with the above XPS results. Crucially, the change of electronic structure between the catalytically active sites of Ni and Fe endows favorable

adsorption/desorption of the oxygen species, thereby promoting oxygen evolution performance and suppressing Fe<sup>3+</sup> dissolution in these vacancy-engineered catalysts [44–46].

In pursuit of an in-depth elucidation of the local electronic structure and coordination environment of Ni<sub>x</sub>Fe<sub>1-x</sub>-LDH@NF ( $x = 0.3, 0.5, 0.7$ ), X-ray absorption spectroscopy (XAS) was performed to explore the coordination number (CN), amorphous state and multi-vacancies of these electrocatalysts. (See the details in Fig. S5 and S6 and Table S1.) As demonstrated in Fig. 3a, the normalized Ni-K X-ray absorption near-edge structure (XANES) spectrum presents that the oxidation state of Ni<sub>0.3</sub>Fe<sub>0.7</sub>-LDH@NF is higher than those of the remaining two electrocatalysts, which agrees well with the XPS results in Fig. 2e. Meanwhile, there is no apparent change in the peak shape in either R or K space in the curves in Fig. 3b and 3c, indicating that the local octahedral structure of Ni is stable; however, the subtle variation of oscillations at high  $k$  values suggests a weak alteration of the coordination environment of the Ni atoms. More specifically, the Fourier transforms (FT) of the extended X-ray absorption fine structure (EXAFS) are available for detailed interpretation regarding Ni coordination, where the peaks at 1.59 Å and 2.72 Å in Fig. 3g could be assigned to the first shell Ni-O and the second shell Ni-Ni/Fe, respectively, and the respective fitting result further manifests the presence of O<sub>v</sub> in Ni<sub>0.3</sub>Fe<sub>0.7</sub>-LDH@NF seeing that the lower CN. Nevertheless, there is a more distinct decline of the Fe valence state for Ni<sub>0.3</sub>Fe<sub>0.7</sub>-LDH@NF in Fig. 4d-f and Fig. 3h, and the Fe K-space possesses much more significant variation than the Ni K-space, demonstrating that evidently varying CN exists in the Fe atoms. Notably, the Ni<sub>0.3</sub>Fe<sub>0.7</sub>-LDH@NF reflects a lowest CN (5.1) of Fe-O at the dominant peak of 1.56 Å, which once again highlights the highest yields of O<sub>v</sub>.

Additionally, another shell could be associated with Fe-Fe/Ni, whose smaller CN suggests more metal vacancies could exist in Ni<sub>0.3</sub>Fe<sub>0.7</sub>-LDH@NF, and as the CN of Fe-Fe/Ni decreased with Fe incorporation, the Fe vacancies would be introduced according to the arrangement of Ni and Fe cations in the basal plane of NiFe-LDH [19,27]. In addition, the signal intensity of electron spin resonance (ESR) (Fig. 3i) at the g values of  $\sim 2.11$  and  $2.23$  also demonstrates the presence of O<sub>v</sub> and Ni<sup>3+</sup>, respectively [47,48]. The modulation of the electronic structure caused by the synergistic effects from the iron and nickel components and greater structural flexibility of multiple-vacancy NiFe-LDH is anticipated to modify the OER mechanism.

### 3.2. Electrocatalytic OER measurement

The electrochemical water oxidation performance of Ni<sub>x</sub>Fe<sub>1-x</sub>-LDH@NF with various Ni/Fe ratios was investigated in 1 M O<sub>2</sub>-saturated KOH solution through a three-electrode setup. As a comparison, commercial IrO<sub>2</sub> was also tested under identical conditions. As presented in Fig. 4a, the Ni<sub>0.3</sub>Fe<sub>0.7</sub>-LDH@NF displays an evidently lower onset potential @ 1 mA·cm<sup>-2</sup> of 1.375 V versus the reversible hydrogen electrode (RHE) than those of the other employed catalysts, facilitating the formation of the reaction intermediate NiFe-OOH. Impressively, the Ni<sub>0.3</sub>Fe<sub>0.7</sub>-LDH@NF exhibits ultralow OER overpotentials (Fig. 4b) of 184, 256, 273 and 287 mV to achieve 10, 100, 200 and 400 mA·cm<sup>-2</sup>, respectively, outperforming the most-often reported catalysts (Table S2).

What's more, the Tafel plots were analyzed to evaluate the kinetics of as-prepared electrodes according to the polarization curves, as displayed in Fig. 4c. Specifically, the Ni<sub>0.3</sub>Fe<sub>0.7</sub>-LDH@NF features a Tafel slope as small as 56.68 mV·dec<sup>-1</sup>, illustrating faster OER reaction kinetics. Moreover, the electrochemical impedance (Fig. 4d) was characterized to further prove the enhanced OER kinetics of Ni<sub>0.3</sub>Fe<sub>0.7</sub>-LDH@NF, where the charge transfer resistance ( $R_{ct}$ ) of Ni<sub>0.3</sub>Fe<sub>0.7</sub>-LDH@NF is the lowest (9.479 Ω·cm<sup>2</sup> @200 mV) among all these samples, indicating it has the fastest charge-transfer for OER, well in accordance with the Tafel analysis. Additionally, the electrochemical surface areas (ECSA) of various specimens were calculated from their double-layer capacitance

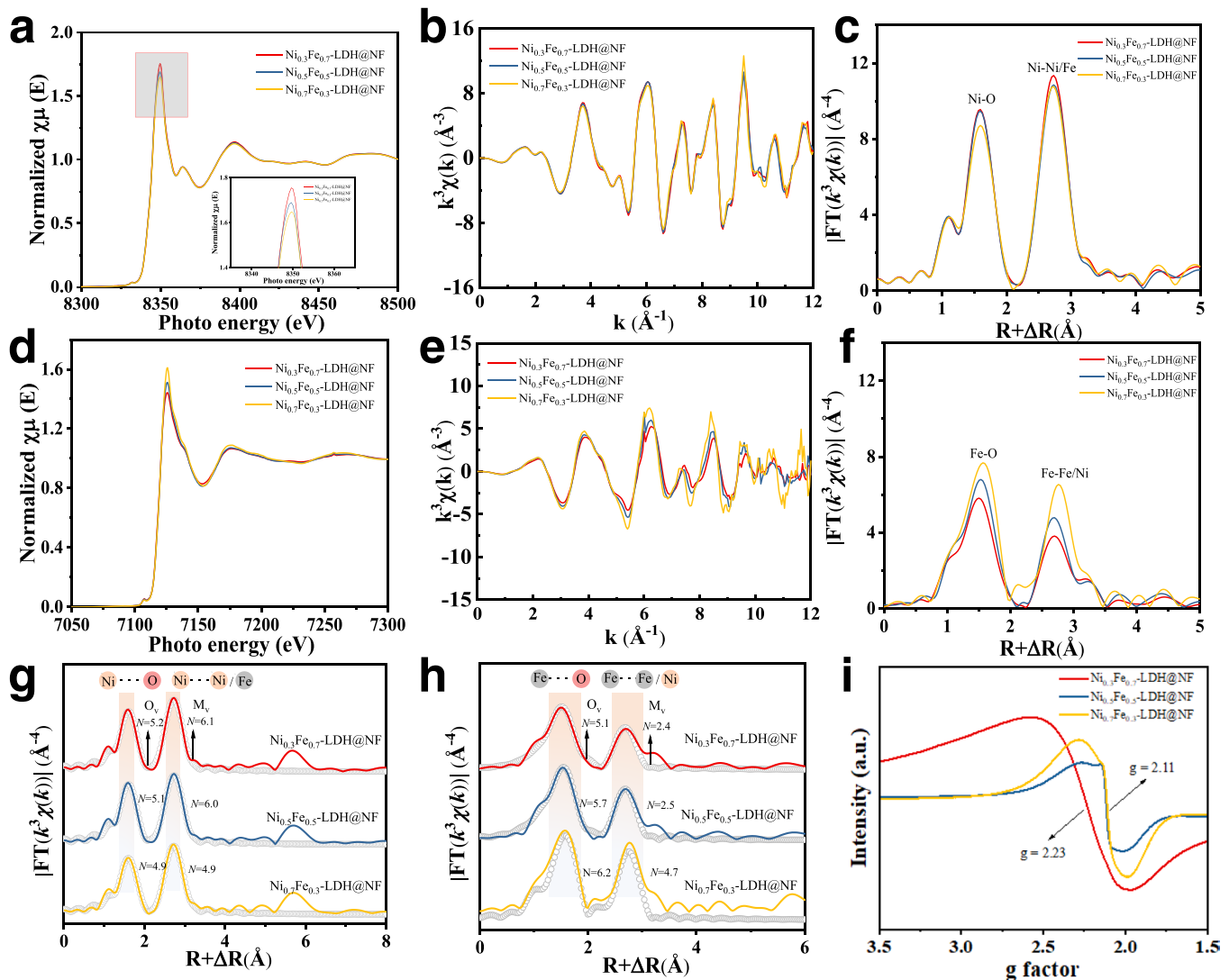


**Fig. 3.** XAS characterization of  $\text{Ni}_x\text{Fe}_{1-x}\text{-LDH@NF}$  ( $x = 0.3, 0.5$  and  $0.7$ ). (a) Ni K-edge XANES. (b) Ni K-edge EXAFS oscillation function  $k^3\chi(k)$ . (c) Ni K-edge FT plots of the EXAFS  $k^3\chi(k)$  function in  $R$ -space. (d) Fe K-edge XANES. (e) Fe K-edge EXAFS oscillation function  $k^3\chi(k)$ . (f) Fe K-edge FT curves of the EXAFS  $k^3\chi(k)$  function in  $R$ -space. The fitted  $R$ -space curves of the (g) Ni K-edge and (h) Fe K-edge. (i) ESR spectra of  $\text{Ni}_x\text{Fe}_{1-x}\text{-LDH@NF}$  ( $x = 0.3, 0.5$  and  $0.7$ ).

( $C_{dl}$ ) on the basis of cyclic voltammetry profiles in a non-faradaic region of 1.125–1.225 V vs. RHE (Fig. S7 and S8). Interestingly, the  $C_{dl}$  of  $\text{Ni}_{0.3}\text{Fe}_{0.7}\text{-LDH@NF}$  is determined to be  $6.66 \text{ mF}\cdot\text{cm}^{-2}$ , which is smaller than those of the other electrodes, as displayed in Fig. 4e. Similarly, this is also the case for the BET results (Fig. S3), which indirectly proved that the intrinsic activity of  $\text{Ni}_{0.3}\text{Fe}_{0.7}\text{-LDH@NF}$ , rather than the surface area, plays an essential role in the OER process. In addition to high OER activity, the stability and durability of  $\text{Ni}_{0.3}\text{Fe}_{0.7}\text{-LDH@NF}$  are also measured, where chronoamperometry (CP) at  $10 \text{ mA}\cdot\text{cm}^{-2}$  and multi-current density CP from  $10$  to  $100 \text{ mA}\cdot\text{cm}^{-2}$  were conducted, as displayed in Fig. 4g. Obviously, the voltage applied after the CP test remains almost unchanged, which suggests considerable stability of  $\text{Ni}_{0.3}\text{Fe}_{0.7}\text{-LDH@NF}$  during the OER process (where  $\text{Ni}_{0.3}\text{Fe}_{0.7}\text{-LDH@NF}$  features excellent structural stability after long-term stability test, Fig. S9). Furthermore, the faradaic efficiency (FE) of  $\text{Ni}_{0.3}\text{Fe}_{0.7}\text{-LDH@NF}$  was obtained via the comparison of theoretical and experimental evolved gas values (Fig. S10), and the  $\text{Ni}_{0.3}\text{Fe}_{0.7}\text{-LDH@NF}$  enables a quite stable oxygen yield rate, indicative of a nearly 100% FE for the OER.

### 3.3. Mechanism analysis

It is known that the variation of pseudocapacitive and OER currents in cyclic voltammetry (CV) plots could be used to evaluate the electrochemical OER performance of the catalysts. A scanning rate from 1 to 10 mV/s for the CV curves was exploited to analyze the kinetics of the electrocatalytic reactions (Fig. 5a-c and Fig. S11,S12). From Fig. 5a, the existence of oxidation peaks at various sweep rates corresponds to the chemical restructuring on the surface of  $\text{Ni}_{0.3}\text{Fe}_{0.7}\text{-LDH@NF}$  preceding the OER process.

In detail, the peak appears at ca. 1.42 V<sub>RHE</sub>, suggesting the phase transformation from NiFe-LDH to active-phase NiOOH [31,47]. Generally, the current ( $i$ ) against sweep rate ( $v$ ) is given by the following formula:

$$i = av^b \quad (3)$$

where the  $b$  value is the slope via linear fitting of the  $\log(i)$  versus  $\log(v)$ , which could be used to elucidate the reaction mechanism. Specifically, the  $b$  value of 0.5 manifests a completely diffusion-controlled process, whereas 1.0 signifies ideally capacitive behavior. As represented in the inset in Fig. 5a, the  $b$  values for the anodic and cathodic peaks are 0.816 and 0.802, respectively, which reveals that the electrochemical kinetics

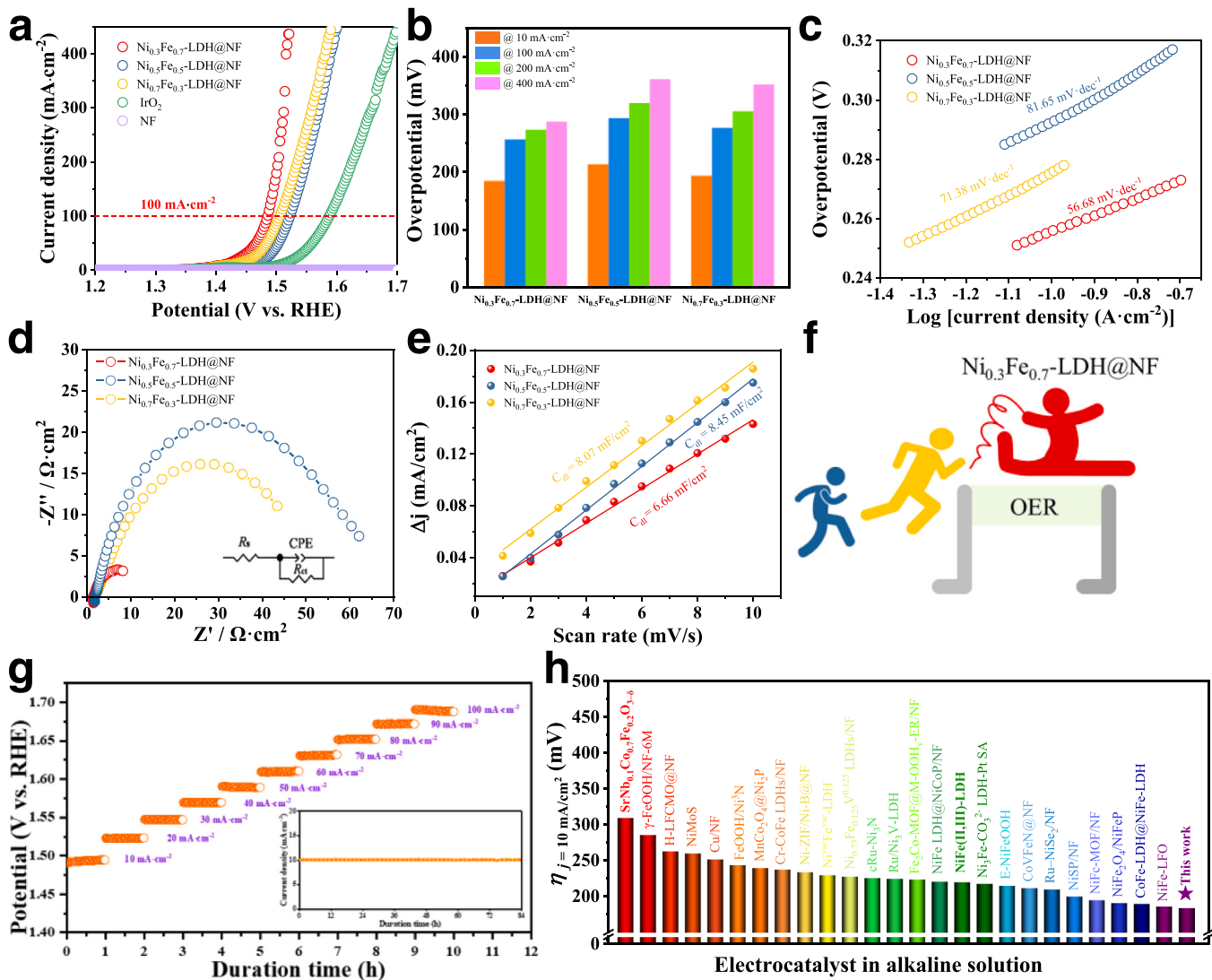


**Fig. 4.** Electrochemical performance of various catalysts in 1 M KOH. (a) Polarization curves. (b) The overpotentials required for  $j = 10, 100, 200$  and  $400 \text{ mA}\cdot\text{cm}^{-2}$  of different specimens. (c) Tafel plots. (d) Nyquist plots at  $1.43 \text{ V}_{\text{RHE}}$ . (e) The  $C_{\text{dl}}$  measurement at the non-faradaic potential window. (f) Schematic diagram of relative performance of the various catalysts. (g) Chronoamperometric plots at multiple current densities from  $10$  to  $100 \text{ mA}\cdot\text{cm}^{-2}$  for  $\text{Ni}_{0.3}\text{Fe}_{0.7}\text{-LDH@NF}$  without iR correction; Inset: @  $10 \text{ mA}\cdot\text{cm}^{-2}$ . (h) Comparison of the overpotentials required at  $10 \text{ mA}\cdot\text{cm}^{-2}$  for the  $\text{Ni}_{0.3}\text{Fe}_{0.7}\text{-LDH@NF}$  with other recently reported electrocatalysts.

is mainly dominated by surface-controlled processes of the  $\text{Ni}_{0.3}\text{Fe}_{0.7}\text{-LDH@NF}$  electrode. Moreover, the specific value of the capacitive contribution at a fixed potential can be further quantified through Eq. 4:

$$i(v) = k_1 v + k_2 v^{1/2} \quad (4)$$

where  $k_1 v$  is attributable to the capacitive portion, while  $k_2 v^{1/2}$  represents the diffusion fraction [49]. Accordingly, 65.19% of the redox current arises from the pseudocapacitive contribution of the  $\text{Ni}_{0.3}\text{Fe}_{0.7}\text{-LDH@NF}$  catalyst at the scan rate of  $5 \text{ mV}\cdot\text{s}^{-1}$  (Fig. 5b), which is higher than those of  $\text{Ni}_{0.5}\text{Fe}_{0.5}\text{-LDH@NF}$  (63.37%) and  $\text{Ni}_{0.7}\text{Fe}_{0.3}\text{-LDH@NF}$  (61.50%) (Fig. S11d and Fig. S12d). In addition, the increment of capacitive contribution ratio with the increasing scanning rate implies that the restricted diffusion behaves with a shorter reaction time (Fig. 5c). Actually, some active sites with high-valence states could be formed via a pseudocapacitive-type intercalation at anodic potentials lower than the OER potential. In our NiFe LDH case, during the pseudocapacitive charging process, the highly active  $\text{NiOOH}$  layer would be formed to participate in the subsequent OER process.

Furthermore, a strong pseudocapacitive behavior signifies massive active centers that are available for diverse redox or intermediate

adsorption reactions over a wide potential window. Therefore, a large pseudocapacitive behavior is usually accompanied by an improved electrocatalytic OER activity, which is reflected by the highest capacitive charge of the  $\text{Ni}_{0.3}\text{Fe}_{0.7}\text{-LDH@NF}$  in Fig. 5d, implying the underlying correlation between pseudocapacitive effect and enhanced OER activity [50–53].

As mentioned previously, the  $\text{Ni}_x\text{Fe}_{1-x}\text{-LDH@NF}$  ( $x = 0.3, 0.5$  and  $0.7$ ) catalysts undergo reconstruction before water oxidation on the surface, and an operando Raman test under OER conditions was conducted in 1 M KOH to further decipher the intrinsic active behavior of  $\text{Ni}_{0.3}\text{Fe}_{0.7}\text{-LDH@NF}$  catalyst. It is generally recognized that the formation of  $\gamma\text{-NiOOH}$  species in NiFe hydroxide is related to the active sites. In Fig. 5e and Fig. S13, strikingly, two characteristic peaks situated at  $300 \text{ cm}^{-1}$  and  $532 \text{ cm}^{-1}$  exhibit apparent blue-shifts with increasing applied potential, which not only indicates the presence of stronger and shorter Fe-O bonds but also the transformation from  $\text{Ni(OH)}_2$  to  $\gamma\text{-NiOOH}$ . Note that the  $\text{Ni}_{0.3}\text{Fe}_{0.7}\text{-LDH@NF}$  only requires  $1.4 \text{ V}$  vs. RHE ( $\text{Ni}_{0.5}\text{Fe}_{0.5}\text{-LDH@NF}$  and  $\text{Ni}_{0.7}\text{Fe}_{0.3}\text{-LDH@NF}$  requires  $1.450 \text{ V}_{\text{RHE}}$  and  $1.425 \text{ V}_{\text{RHE}}$ , respectively, Fig. S14 and Fig. S15), which is lower than the reported NiFe-LDH electrocatalyst and demonstrates that it possesses

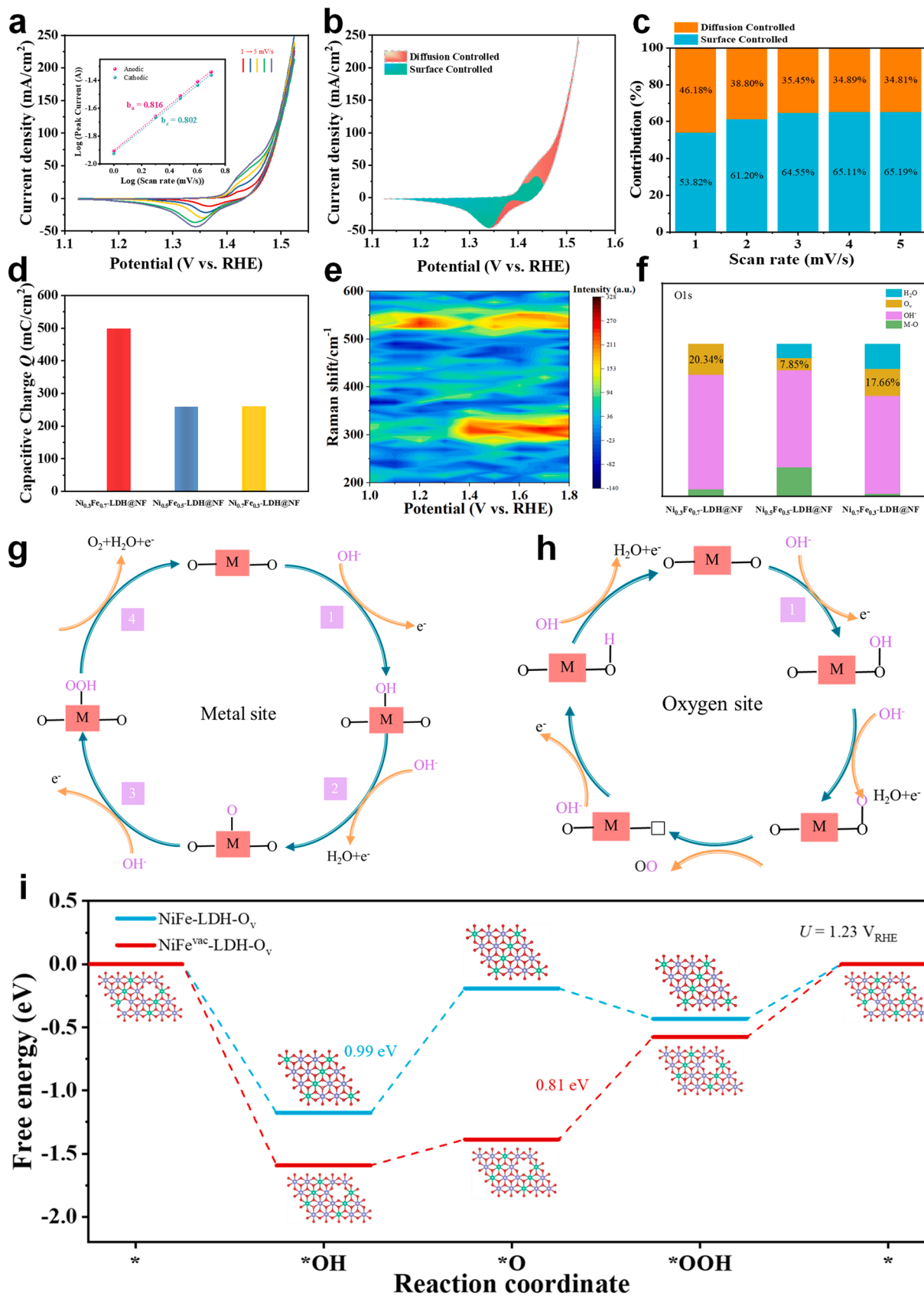


**Fig. 5.** Electrochemical kinetics analyses of Ni<sub>0.3</sub>Fe<sub>0.7</sub>-LDH@NF. (a) CV curves at various scan rates from 1 to 5 mV/s. Inset:  $b$ -value determination. (b) Capacitive contribution and diffusion contribution at a scanning rate of 5 mV/s. (c) Contribution ratios of the capacitive and diffusion-controlled charge vs. scan rate. (d) Capacitive charge. (e) Operando Raman of Ni<sub>0.3</sub>Fe<sub>0.7</sub>-LDH@NF from 1.0 V<sub>RHE</sub> to 1.8 V<sub>RHE</sub>. (f) The contribution of different oxygen-containing groups after OER testing. OER mechanisms of Ni<sub>0.3</sub>Fe<sub>0.7</sub>-LDH@NF: (g) Adsorbate evolution mechanism (AEM) and (h) Lattice-oxygen oxidation mechanism (LOM). (i) Free energies of OER steps via LOM on different NiFe-LDH surfaces. Green, purple, red, and light pink balls represent nickel, iron, oxygen, and hydrogen atoms, respectively.

faster kinetics due to the structural flexibility endowed by a high content of multiple vacancies, corresponding to a smaller overpotential ascribed to the LSV curve [46]. Additionally, the XRD patterns of all the samples after OER (Fig. S16a) still reveal the presence of NiFe-LDHs, while the TEM images of  $\text{Ni}_{0.3}\text{Fe}_{0.7}\text{-LDH@NF}$  after OER also verify that the catalyst surface undergoes the restructuring process, producing amorphous  $\gamma\text{-NiOOH}$  (Fig. S17) [54,55].

The Tafel slope of  $56.68 \text{ mV}\cdot\text{dec}^{-1}$  determined for  $\text{Ni}_{0.3}\text{Fe}_{0.7}\text{-LDH@NF}$  indicates that the rate-determining step (RDS) is the transformation from M-O into M-OOH (the third step) [56]. The classic adsorbate evolution mechanism (AEM) may not be the only governing mechanism during this OER process, given that the minimum thermodynamic overpotential is  $\sim 0.37 \text{ V}$  in AEM, while the overpotential for our  $\text{Ni}_{0.3}\text{Fe}_{0.7}\text{-LDH@NF}$  is only  $0.18 \text{ V}$ . The rapid OER kinetics of  $\text{Ni}_{0.3}\text{Fe}_{0.7}\text{-LDH@NF}$  possessing multiple vacancies is assisted by the active-site layer formed by oxygen-vacancy-mediated redox pseudocapacitance, which enables facile oxygen intercalation at surface  $\text{O}_v$  using  $\text{OH}^-$  as the intercalating ion, achieving the participation of surface lattice-oxygen under OER conditions. Coincidentally, the pH-dependence of OER activity and the location of redox peaks on the RHE scale of  $\text{Ni}_x\text{Fe}_{1-x}\text{-LDH@NF}$  ( $x = 0.3, 0.5$  and  $0.7$ ) (Fig. S18) implies the lattice-oxygen oxidation mechanism (LOM) in water oxidation [9]. Meanwhile, the content of  $\text{O}_v$  species derived from the high-resolution O 1s spectra of as-prepared catalysts after OER testing (Fig. 5f and Fig. S16b) further confirms that the  $\text{Ni}_{0.3}\text{Fe}_{0.7}\text{-LDH@NF}$  possesses more oxygen vacancies than the other catalysts, implying that it is easier to trigger lattice-oxygen oxidation during the OER [57].

Based on the above analysis, besides the conventional AEM (Fig. 5g), one possible LOM pathway involving five intermediate states was proposed for the OER process on our NiFe LDH catalysts. The sequential intermediates are M-OH, M-O, M-OOH, M-OO and M-◻ (here **O** in bold represents the oxygen active site, and ◻ indicates the oxygen vacancy), as schematically displayed in Fig. 5 h. The multiple vacancy defects in  $\text{Ni}_{0.3}\text{Fe}_{0.7}\text{-LDH@NF}$  enhance the intrinsic flexibility of the NiFe-LDH structure, which is conducive to both facilitating the surface-reconstructed active oxyhydroxide species (AEM pathway) and activating lattice-oxygen oxidation under the OER process accompanied by the formation of oxygen vacancies (LOM pathway). It should be noted that oxygen vacancies will be easily attacked by medium  $\text{OH}^-$ , featuring anion-based intercalation pseudocapacitance that substantially promotes the OER kinetics.

To fundamentally elucidate the synergic effect of multiple vacancies in  $\text{Ni}_{0.3}\text{Fe}_{0.7}\text{-LDH@NF}$  on lattice oxygen oxidation, the Gibbs free energy ( $\Delta G$ ) of  $\text{Ni}_{0.3}\text{Fe}_{0.7}\text{-LDH@NF}$  with two structural models was calculated DFT ( $U = 1.23 \text{ V}$ ), as demonstrated in Fig. 5i. In terms of the  $\text{Ni}_{0.3}\text{Fe}_{0.7}\text{-LDH@NF}$  containing only  $\text{O}_v$ , the formation of M-O serves as the RDS due to the highest free energy ( $\Delta G_{\text{RDS}}$ ) of  $0.99 \text{ eV}$  in the second step of OER; while the computed thermodynamical potential necessary for LOM pathway was found to become remarkably favorable assisted by the incorporation of Fe vacancies, which displays the smaller  $\Delta G_{\text{RDS}}$  of  $0.81 \text{ eV}$  in the forming of M-OOH, consistent with the Tafel analysis and operando Raman test. This transformation of RDS verifies that the integration of oxygen and iron vacancies on  $\text{Ni}_{0.3}\text{Fe}_{0.7}\text{-LDH@NF}$  effectively diminishes the binding energies of oxygen-containing intermediates in LOM pathway, further optimizing the evolution of active sites (Fig. S19) [58]. Hence, the  $\text{Ni}_{0.3}\text{Fe}_{0.7}\text{-LDH@NF}$  material endowed with multiple vacancies would follow the AEM together with LOM kinetics during water oxidation, exhibiting extraordinary OER performance (Fig. S20, Table S3) [57,59–61].

#### 4. Conclusions

In summary, we have demonstrated a strategy for integration of the oxygen and iron vacancies to fabricate NiFe LDH nanosheets with different proportions of Ni and Fe grown on NF via a simple one-step hydrothermal method. The union of oxygen and Fe vacancies on

$\text{Ni}_{0.3}\text{Fe}_{0.7}\text{-LDH@NF}$  enriches the coordinatively unsaturated sites and boosts the adsorption of oxygenated intermediates in LOM pathway, significantly enhancing the activity of the NiFe-LDH structure for the OER. Operando electrochemical Raman characterization and OER kinetic analysis reveal that  $\text{O}_v$ -induced  $\text{NiOOH}$  intermediate species are associated with oxygen-ion-based intercalation pseudocapacitance, activating the LOM pathway during water oxidation. Our findings shed light on the rational design of novel electrocatalysts with multiple vacancy types for efficient water oxidation or other energy-conversion reactions containing oxygen vacancies.

#### CRediT authorship contribution statement

**Yiyue Zhai:** Methodology, Investigation, Data curation, Formal analysis, Writing - original draft. **Xiangrong Ren:** Data curation, Formal analysis, Writing - review & editing. **Yu Sun:** DFT calculation, Formal analysis. **Deng Li:** Writing - review & editing. **Bolun Wang:** Investigation, Visualization, Writing - review & editing, Supervision. **Shengzhong (Frank) Liu:** Conceptualization, Visualization, Writing - review & editing, Supervision, Project administration, Funding acquisition.

#### Declaration of Competing Interest

The authors declare that they have no known competing financial interests or personal relationships that could have appeared to influence the work reported in this paper.

#### Data availability

Data will be made available on request.

#### Acknowledgments

We sincerely thank Prof. Jiaxing Jiang for his help with BET testing. We appreciate the funding support from the 111 Project (Grant No. B21005), the National Key Research Program of China (2017YFA0204800, 2016YFA0202403), the National Natural Science Foundation of China (Grant No. 22205073), and the Fundamental Research Funds for the Central Universities (2020TS104, 2021TS003).

#### Appendix A. Supplementary data

Supplementary material related to this article can be found, in the online version, at doi:10.1016/j.apcatb.2022.122091.

#### References

- [1] Y. Wang, S. Wang, Z.L. Ma, L.T. Yan, X.B. Zhao, Y.Y. Xue, J.M. Huo, X. Yuan, S. N. Li, Q.G. Zhai, Competitive coordination-oriented monodispersed ruthenium sites in conductive MOF/LDH heteronano-tree catalysts for efficient overall water splitting in alkaline media, *Adv. Mater.* (2022), 2107488.
- [2] C. Wang, P.L. Zhai, M.Y. Xia, Y.Z. Wu, B. Zhang, Z.W. Li, L. Ran, J.F. Gao, X. M. Zhang, Z.Z. Fan, L.C. Sun, J.G. Hou, Engineering lattice oxygen activation of iridium clusters stabilized on amorphous bimetal borides array for oxygen evolution reaction, *Angew. Chem. Int. Ed.* 60 (2021) 27126–27134.
- [3] P. Liu, B. Chen, C.W. Liang, W.T. Yao, Y.Z. Cui, S.Y. Hu, P.C. Zou, H. Zhang, H. J. Fan, C. Yang, Tip-enhanced electric field: a new mechanism promoting mass transfer in oxygen evolution reactions, *Adv. Mater.* 33 (2021), 2007377.
- [4] S.F. Sun, X. Zhou, B.W. Cong, W.Z. Hong, G. Chen, Tailoring the d-band centers endows  $(\text{Ni}_x\text{Fe}_{1-x})_2\text{P}$  nanosheets with efficient oxygen evolution catalysis, *ACS Catal.* 10 (2020) 9086–9097.
- [5] N. Zhang, X.B. Feng, D.W. Rao, X. Deng, L.J. Cai, B.C. Qiu, R. Long, Y.J. Xiong, Y. Lu, Y. Chai, Lattice oxygen activation enabled by high-valence metal sites for enhanced water oxidation, *Nat. Commun.* 11 (2020) 4066.
- [6] Y.L. Zhu, H.A. Tahini, Z.W. Hu, Z.G. Chen, W. Zhou, A.C. Komarek, Q. Lin, H.J. Lin, C.T. Chen, Y.J. Zhong, M.T. Fernandez-Diaz, S.C. Smith, H.T. Wang, M.L. Liu, Z. P. Shao, Boosting oxygen evolution reaction by creating both metal ion and lattice-oxygen active sites in a complex oxide, *Adv. Mater.* 32 (2020), 1905025.
- [7] J. Zhou, L.J. Zhang, Y.C. Huang, C.L. Dong, H.J. Lin, C.T. Chen, L.H. Tjeng, Z. W. Hu, Voltage- and time-dependent valence state transition in cobalt oxide catalysts during the oxygen evolution reaction, *Nat. Commun.* 11 (2020) 1984.

- [8] H. Sun, L. Chen, Y.B. Lian, W.J. Yang, L. Lin, Y.F. Chen, J.B. Xu, D. Wang, X. Q. Yang, M.H. Rummerli, J. Guo, J. Zhong, Z. Deng, Y. Jiao, Y. Peng, S.Z. Qiao, Transformed polygonal mesopores on ternary layered double hydroxides exposing under-coordinated metal centers for accelerated water dissociation, *Adv. Mater.* 32 (2020), 2006784.
- [9] S.B. Liu, C. Sun, J. Chen, J. Xiao, J.L. Luo, Ruddlesden-Popper perovskite for bifunctional oxygen electrocatalysis, *ACS Catal.* 10 (2020) 13437–13444.
- [10] L.H. Zhuang, L. Ge, Y.S. Yang, M.R. Li, Y. Jia, X.D. Yao, Z.H. Zhu, Ultrathin iron-cobalt oxide nanosheets with abundant oxygen vacancies for the oxygen evolution reaction, *Adv. Mater.* 29 (2017), 1606793.
- [11] J.Y. Zhang, Y. Yan, B.B. Mei, R.J. Qi, T. He, Z.T. Wang, W.S. Fang, S. Zaman, Y. Q. Su, S.J. Ding, B.Y. Xia, Local spin-state tuning of cobalt-iron selenide nanoframes for the boosted oxygen evolution, *Energy Environ. Sci.* 14 (2021) 365–373.
- [12] C. Chen, Y.X. Tuo, Q. Lu, H. Lu, S.Y. Zhang, Y. Zhou, J. Zhang, Z.N. Liu, Z.X. Kang, X. Feng, D. Chen, Hierarchical trimetallic Co-Ni-Fe oxides derived from core-shell structured metal-organic frameworks for highly efficient oxygen evolution reaction, *Appl. Catal. B Environ.* 287 (2021), 119953.
- [13] J.D. Chen, F. Zheng, S.J. Zhang, A. Fisher, Y. Zhou, Z.Y. Wang, Y.Y. Li, B.B. Xu, J. T. Li, S.G. Sun, Interfacial interaction between FeOOH and Ni-Fe LDH to modulate the local electronic structure for enhanced OER electrocatalysis, *ACS Catal.* 8 (2018) 11342–11351.
- [14] R. Chen, S.F. Hung, D.J. Zhou, J.J. Gao, C.J. Yang, H.B. Tao, H.B. Yang, L.P. Zhang, L.L. Zhang, Q.H. Xiong, H.M. Chen, B. Liu, Layered structure causes bulk NiFe layered double hydroxide unstable in alkaline oxygen evolution reaction, *Adv. Mater.* 31 (2019), 1903909.
- [15] D.J. Zhou, S.Y. Wang, Y. Jia, X.Y. Xiong, H.B. Yang, S. Liu, J.L. Tang, J.M. Zhang, D. Liu, L.R. Zheng, Y. Kuang, X.M. Sun, B. Liu, NiFe hydroxide lattice tensile strain: enhancement of adsorption of oxygenated intermediates for efficient water oxidation catalysis, *Angew. Chem. Int. Ed.* 58 (2019) 736–740.
- [16] L. Yu, H.Q. Zhou, J.Y. Sun, I.K. Mishra, D. Luo, F. Yu, Y. Yu, S. Chen, Z.F. Ren, Amorphous NiFe layered double hydroxide nanosheets decorated on 3D nickel phosphide nanoarrays: a hierarchical core-shell electrocatalyst for efficient oxygen evolution, *J. Mater. Chem. A* 6 (2018) 13619–13623.
- [17] Y.F. Zhao, X. Zhang, X.D. Jia, G.I.N. Waterhouse, R. Shi, X.R. Zhang, F. Zhan, Y. Tao, L.Z. Wu, C.H. Tung, D. O'Hare, T.R. Zhang, Sub-3 nm ultrafine monolayer layered double hydroxide nanosheets for electrochemical water oxidation, *Adv. Energy Mater.* 8 (2018), 1703585.
- [18] L.Y. Hu, X. Zeng, X.Q. Wei, H.J. Wang, Y. Wu, W.L. Gu, L. Shi, C.Z. Zhu, Interface engineering for enhancing electrocatalytic oxygen evolution of NiFe LDH/NiTe heterostructures, *Appl. Catal. B Environ.* 273 (2020), 119014.
- [19] Y.Q. Wang, S. Tao, H. Lin, G.P. Wang, K.N. Zhao, R.M. Cai, K.W. Tao, C.X. Zhang, M.Z. Sun, J. Hu, B.L. Huang, S.H. Yang, Atomically targeting NiFe LDH to create multivacancies for OER catalysis with a small organic anchor, *Nano Energy* 81 (2021), 105606.
- [20] J.F. Zhang, J.Y. Liu, L.F. Xi, Y.F. Yu, N. Chen, S.H. Sun, W.C. Wang, K.M. Lange, B. Zhang, Single-atom Au/NiFe layered double hydroxide electrocatalyst: probing the origin of activity for oxygen evolution reaction, *J. Am. Chem. Soc.* 140 (2018) 3876–3879.
- [21] C.L. Li, Z.J. Zhang, R. Liu, In situ growth of 3D NiFe LDH-POM micro-flowers on nickel foam for overall water splitting, *Small* 16 (2020), 2003777.
- [22] B.R. Wang, S.H. Jiao, Z.S. Wang, M.J. Lu, D. Chen, Y.T. Kang, G.S. Pang, S.H. Feng, Rational design of NiFe LDH@Ni<sub>3</sub>N nano/microsheet arrays as a bifunctional electrocatalyst for overall water splitting, *J. Mater. Chem. A* 8 (2020) 17202–17211.
- [23] G.B. Chen, T. Wang, J. Zhang, P. Liu, H.J. Sun, X.D. Zhuang, M.W. Chen, X.L. Feng, Accelerated hydrogen evolution kinetics on NiFe-layered double hydroxide electrocatalysts by tailoring water dissociation active sites, *Adv. Mater.* 30 (2018), 1706279.
- [24] Z.X. Xu, Y.R. Ying, G.G. Zhang, K.Z. Li, Y. Liu, N.Q. Fu, X.Y. Guo, F. Yu, H. T. Huang, Engineering NiFe layered double hydroxide by valence control and intermediate stabilization toward the oxygen evolution reaction, *J. Mater. Chem. A* 8 (2020) 26130–26138.
- [25] H.Z. Zhong, G.P. Gao, X.N. Wang, H.Y. Wu, S.H. Shen, W.B. Zuo, G.X. Cai, G. Wei, Y. Shi, D.J. Fu, C.Z. Jiang, L.W. Wang, F. Ren, Ion irradiation inducing oxygen vacancy-rich NiO/NiFe<sub>2</sub>O<sub>4</sub> heterostructure for enhanced electrocatalytic water splitting, *Small* 17 (2021), 2103501.
- [26] Y. Zhang, J.L. Fu, H. Zhao, R.J. Jiang, F. Tian, R.J. Zhang, Tremella-like Ni<sub>3</sub>S<sub>2</sub>/MnS with ultrathin nanosheets and abundant oxygen vacancies directly used for high speed overall water splitting, *Appl. Catal. B Environ.* 257 (2019) 17899.
- [27] B. Liu, Y. Wang, H.Q. Peng, R.O. Yang, Z. Jiang, X.T. Zhou, C.S. Lee, H.J. Zhao, W. J. Zhang, Iron vacancies induced bifunctionality in ultrathin ferroxyhyte nanosheets for overall water splitting, *Adv. Mater.* 30 (2018), 1803144.
- [28] Y.Y. Wang, Y.Q. Zhang, Z.J. Liu, C. Xie, S. Feng, D.D. Liu, M.F. Shao, S.Y. Wang, Layered double hydroxide nanosheets with multiple vacancies obtained by dry exfoliation as highly efficient oxygen evolution electrocatalysts, *Angew. Chem. Int. Ed.* 56 (2017) 5867–5871.
- [29] X.Q. Du, Z. Yang, Y. Li, Y.Q. Gong, M. Zhao, Controlled synthesis of Ni(OH)<sub>2</sub>/Ni<sub>3</sub>S<sub>2</sub> hybrid nanosheet arrays as highly active and stable electrocatalysts for water splitting, *J. Mater. Chem. A* 6 (2018) 6938–6946.
- [30] F.M. Wang, J.W. Chen, X.P. Qi, H. Yang, H.H. Jiang, Y.Q. Deng, T.X. Liang, Increased nucleation sites in nickel foam for the synthesis of MoP@Ni<sub>3</sub>P/NF nanosheets for bifunctional water splitting, *Appl. Surf. Sci.* 481 (2019) 1403–1411.
- [31] L. Cheng, M. Xu, Q.S. Zhang, G.C. Li, J.X. Chen, Y.B. Lou, NH<sub>4</sub>F assisted and morphology-controlled fabrication of ZnCo<sub>2</sub>O<sub>4</sub> nanostructures on Ni-foam for enhanced energy storage devices, *J. Alloy. Compd.* 781 (2019) 245–254.
- [32] Y. Luo, Y.H. Wu, D.H. Wu, C. Huang, D.Z. Xiao, H.Y. Chen, S.L. Zheng, P.K. Chu, NiFe-layered double hydroxide synchronously activated by heterojunctions and vacancies for the oxygen evolution reaction, *ACS Appl. Mater. Inter.* 12 (2020) 42850–42858.
- [33] Y.P. Lin, H. Wang, C.K. Peng, L.M. Bu, C.L. Chiang, K. Tian, Y. Zhao, J.Q. Zhao, Y. G. Lin, J.M. Lee, L.J. Gao, Co-induced electronic optimization of hierarchical NiFe LDH for oxygen evolution, *Small* 16 (2020), 2002426.
- [34] M. Ishizaki, H. Tanno, H. Sutoh, T. Katsuki, T. Hayasaka, M. Yagi, Y. Tsubonouchi, K. Tajima, T. Kawamoto, Y. Sakuda, M. Kurihara, FeNi-layered double-hydroxide nanoflakes with potential for intrinsically high water-oxidation catalytic activity, *ACS Appl. Energy Mater.* 3 (2020) 9040–9050.
- [35] Y.J. Wu, J. Yang, T.X. Tu, W.Q. Li, P.F. Zhang, Y. Zhou, J.F. Li, J.T. Li, S.G. Sun, Evolution of cationic vacancy defects a motif for surface restructuration of OER precatalyst, *Angew. Chem. Int. Ed.* 60 (2021) 26829–26836.
- [36] S.M. Yin, W.G. Tu, Y. Sheng, Y.H. Du, M. Kraft, A. Borgna, R. Xu, A highly efficient oxygen evolution catalyst consisting of interconnected nickel-iron-layered double hydroxide and carbon nanodomains, *Adv. Mater.* 30 (2018), 1705106.
- [37] Y. Liang, J. Wang, D.P. Liu, L. Wu, T.Z. Li, S.C. Yan, Q. Fan, K. Zhu, Z.G. Zou, Ultrafast Fenton-like reaction route to FeOOH/NiFe-LDH heterojunction electrode for efficient oxygen evolution reaction, *J. Mater. Chem. A* 9 (2021) 21785–21791.
- [38] Y. Du, D.P. Liu, T.Z. Li, Y.D. Yan, Y. Liang, S.C. Yan, Z.G. Zou, A phase transformation-free redox couple mediated electrocatalytic oxygen evolution reaction, *Appl. Catal. B Environ.* 306 (2022), 121146.
- [39] J. Kwon, H. Han, S. Jo, S. Choi, K.Y. Chung, G. Ali, K. Park, U. Paik, T. Song, Amorphous nickel-iron borophosphate for a robust and efficient oxygen evolution reaction, *Adv. Energy Mater.* 11 (2021), 2100624.
- [40] Y.M. Sun, S.N. Sun, H.T. Yang, S.B. Xi, J. Gracia, Z.C.J. Xu, Spin-related electron transfer and orbital interactions in oxygen electrocatalysis, *Adv. Mater.* 32 (2020), 2003297.
- [41] H.Y. Zhao, Y.J. Wang, Y.B. Wang, T.C. Cao, G.H. Zhao, Electro-Fenton oxidation of pesticides with a novel Fe<sub>3</sub>O<sub>4</sub>@Fe<sub>2</sub>O<sub>3</sub>/activated carbon aerogel cathode: High activity, wide pH range and catalytic mechanism, *Appl. Catal. B Environ.* 125 (2012) 120–127.
- [42] Y.H. Tang, Q. Liu, L. Dong, H.B. Wu, X.Y. Yu, Activating the hydrogen evolution and overall water splitting performance of NiFe LDH by cation doping and plasma reduction, *Appl. Catal. B Environ.* 266 (2020), 118627.
- [43] B. Fei, Z.L. Chen, J.X. Liu, H.B. Xu, X.X. Yan, H.L. Qing, M. Chen, R. Wu, Ultrathinning nickel sulfide with modulated electron density for efficient water splitting, *Adv. Energy Mater.* 10 (2020), 2001963.
- [44] G.L. Fu, W.W. Li, J.Y. Zhang, M.S. Li, C.J. Li, N. Li, Q. He, S.B. Xi, D.C. Qi, J. L. MacManus-Driscoll, J. Cheng, K.H. Zhang, Facilitating the deprotonation of OH to O through Fe<sup>4+</sup>-induced states in perovskite LaNiO<sub>3</sub> enables a fast oxygen evolution reaction, *Small* 17 (2021), 2006930.
- [45] M.J. Liu, K.A. Min, B. Han, L.Y.S. Lee, Interfacing or doping? Role of Ce in highly promoted water oxidation of NiFe-layered double hydroxide, *Adv. Energy Mater.* 11 (2021), 2101281.
- [46] L.S. Peng, N. Yang, Y.Q. Yang, Q. Wang, X.Y. Xie, D.X. Sun-Waterhouse, L. Shang, T.R. Zhang, G.I.N. Waterhouse, Atomic cation-vacancy engineering of NiFe-layered double hydroxides for improved activity and stability towards the oxygen evolution reaction, *Angew. Chem. Int. Ed.* 60 (2021) 24612–24619.
- [47] Z.Y. Zhao, Q. Shao, J.Y. Xue, B.L. Huang, Z. Niu, H.W. Gu, X.Q. Huang, J.P. Lang, Multiple structural defects in ultrathin NiFe-LDH nanosheets synergistically and remarkably boost water oxidation reaction, *Nano Res.* 15 (2021) 310–316.
- [48] X. Zhang, Y.F. Zhao, Y.X. Zhao, R. Shi, G.I.N. Waterhouse, T.R. Zhang, A simple synthetic strategy toward defect-rich porous monolayer NiFe-layered double hydroxide nanosheets for efficient electrocatalytic water oxidation, *Adv. Energy Mater.* 9 (2019), 1900881.
- [49] L. Zhang, X.H. Zhang, G.Y. Tian, Q.H. Zhang, M. Knapp, H. Ehrenberg, G. Chen, Z. X. Shen, G.C. Yang, L. Gu, F. Du, Lithium lanthanum titanate perovskite as an anode for lithium ion batteries, *Nat. Commun.* 11 (2020) 3490.
- [50] W.J. Liu, X. Hu, H.C. Li, H.Q. Yu, Pseudocapacitive Ni-Co-Fe hydroxides/N-doped carbon nanoplates-based electrocatalyst for efficient oxygen evolution, *Small* 14 (2018), 1801878.
- [51] S.H. Yan, K.P. Abhilash, L.Y. Tang, M. Yang, Y.F. Ma, Q.Y. Xia, Q.B. Guo, H. Xia, Research advances of amorphous metal oxides in electrochemical energy storage and conversion, *Small* 15 (2019), 1804371.
- [52] H.L. Jiang, Q. He, X.Y. Li, X.Z. Su, Y.K. Zhang, S.M. Chen, S. Zhang, G.Z. Zhang, J. Jiang, Y. Luo, P.M. Ajayan, L. Song, Tracking structural self-reconstruction and identifying true active sites toward cobalt oxychloride precatalyst of oxygen evolution reaction, *Adv. Mater.* 31 (2019), 1805127.
- [53] X.R. Ren, Y.Y. Zhai, Q. Zhou, J.Q. Yan, S.Z. Liu, Fabrication of nanoporous Ni and NiO via a dealloying strategy for water oxidation catalysis, *J. Energy Chem.* 50 (2020) 125–134.
- [54] N.C.S. Selvam, L.J. Du, B.Y. Xia, P.J. Yoo, B. You, Reconstructed water oxidation electrocatalysts: the impact of surface dynamics on intrinsic activities, *Adv. Funct. Mater.* 31 (2020), 2008190.
- [55] Y. Sun, R. Li, X.X. Chen, J. Wu, Y. Xie, X. Wang, K.K. Ma, L. Wang, Z. Zhang, Q. Liao, Z. Kang, Y. Zhang, A-site management prompts the dynamic reconstructed active phase of perovskite oxide OER catalysts, *Adv. Energy Mater.* 11 (2021), 2003755.
- [56] D.R. Kauffman, D. Alfonso, D.N. Tafen, J. Lekse, C.J. Wang, X.Y. Deng, J. Lee, H. Jang, J.S. Lee, S. Kumar, C. Matranga, Electrocatalytic oxygen evolution with an atomically precise nickel catalyst, *ACS Catal.* 6 (2016) 1225–1234.
- [57] J.T. Mefford, X. Rong, A.M. Abakumov, W.G. Hardin, S. Dai, A.M. Kolpak, K. P. Johnston, K.J. Stevenson, Water electrolysis on La<sub>1-x</sub> Sr<sub>x</sub> CoO<sub>3-δ</sub> perovskite electrocatalysts, *Nat. Commun.* 7 (2016) 11053.

- [58] N. Zhang, Y. Chai, Lattice oxygen redox chemistry in solid-state electrocatalysts for water oxidation, *Energy Environ. Sci.* 14 (2021) 4647–4671.
- [59] F.Y. Chen, Z.Y. Wu, Z. Adler, H.T. Wang, Stability challenges of electrocatalytic oxygen evolution reaction: From mechanistic understanding to reactor design, *Joule* 5 (2021) 1704–1731.
- [60] J.X. Chen, Q.W. Long, K. Xiao, T. Ouyang, N. Li, S.Y. Ye, Z.Q. Liu, Vertically-interlaced NiFeP/MXene electrocatalyst with tunable electronic structure for high-efficiency oxygen evolution reaction, *Sci. Bull.* 66 (2021) 1063–1072.
- [61] T.W. Zhao, Y. Wang, S. Karuturi, K. Catchpole, Q. Zhang, C. Zhao, Design and operando/in situ characterization of precious-metal-free electrocatalysts for alkaline water splitting, *Carbon Energy* 2 (2020) 582–613.